ACS NANO

www.acsnano.org

ARTICLE

Probing Nanotopography-Mediated Macrophage Polarization via Integrated Machine Learning and Combinatorial Biophysical Cue Mapping

Yannan Hou, Brandon Conklin, Hye Kyu Choi, Letao Yang,* and Ki-Bum Lee*

Cite This: *ACS Nano* 2024, 18, 25465−25477

Read Online

ACCESS | Metrics & More | Article Recommendations | Supporting Information

ABSTRACT: **Inflammatory responses, leading to fibrosis and potential host rejection, significantly hinder the long-term success and widespread adoption of biomedical implants. The ability to control and investigated macrophage inflammatory responses at the implant-macrophage interface would be critical for reducing chronic inflammation and improving tissue integration. Nonetheless, the systematic investigation of how surface topography affects macrophage polarization is typically complicated by the restricted complexity of accessible nanostructures, difficulties in achieving exact control, and biased preselection of experimental parameters. In response to these problems, we developed a large-scale, high-content combinatorial biophysical cue (CBC) array for enabling high-throughput screening (HTS) of the effects of nanotopography on macrophage polarization and subsequent inflammatory processes. Our CBC array, created utilizing the dynamic laser interference lithography (DLIL) technology, contains over 1 million nanotopographies, ranging from nanolines and nanogrids to intricate hierarchical structures with dimensions ranging from 100 nm to several microns. Using machine learning (ML) based on the Gaussian process regression algorithm, we successfully identified certain topographical signals that either repress (pro-M2) or stimulate (pro-M1) macrophage polarization. The upscaling of these nanotopographies for further examination has shown mechanisms such as cytoskeletal remodeling and ROCK-dependent epigenetic activation to be critical to the mechanotransduction pathways regulating macrophage fate. Thus, we have also developed a platform combining advanced DLIL nanofabrication techniques, HTS, ML-driven prediction of nanobio interactions, and mechanotransduction pathway evaluation. In short, our developed platform technology not only improves our ability to investigate and understand nanotopography-regulated macrophage inflammatory responses but also holds great potential for guiding the design of nanostructured coatings for therapeutic biomaterials and biomedical implants.**

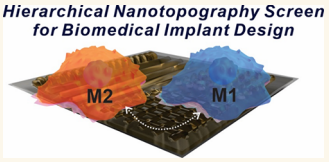

KEYWORDS: *nanotopography-mediated macrophage polarization, combinatorial biophysical cues, machine-learning-driven analysis, immunomodulation, high-throughput screening, epigenetic modulation*

INTRODUCTION

In modern medicine, biomedical implants, such as metal bone grafts, neural interfaces, pacemakers, and intrathecal pumps, play a vital role in restoring functionality and enhancing the patient's quality of life. However, the success of these implants hinges on their interaction with the body at the nanoscale level, often referred to as the nanobio interface.[1] The interface between the implant and the host tissue plays a crucial role in determining the extent of implant integration and tissue regeneration.[2−7] Ideally, the implants should be engineered to elicit specific cellular responses that promote integration and regeneration such as cellular adhesion, proliferation, and modulation of cellular behavior. Conversely, if the immune system reacts negatively with the implanted biomaterial, it can trigger chronic inflammation. This inflammatory response can lead to fibrosis, a process where scar tissue builds up around the implant, and ultimately to rejection by the host's body.[8,9] These complications can significantly compromise or entirely negate the intended function of the implant.[10,11]

To tackle the challenges outlined above, there is a clear interest in devising effective strategies aimed at engineering the microenvironments. These engineered microenvironments can mitigate inflammatory responses while simultaneously fostering tissue repair and regeneration.[12] Despite these efforts, translating such approaches into clinical applications continues

Received: April 2, 2024
Revised: August 26, 2024
Accepted: August 29, 2024
Published: September 3, 2024

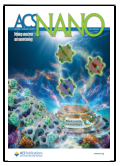

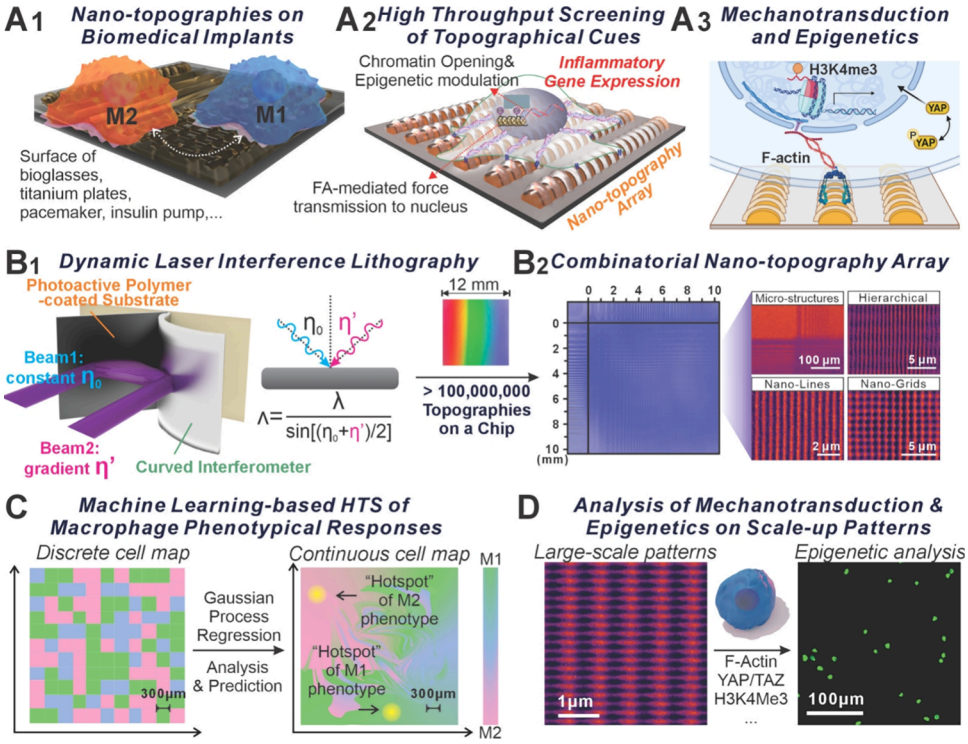

Figure 1. High-throughput screening (HTS) and machine-learning-based analysis of nanobio interfaces for induced macrophage inflammatory responses using nanotopography arrays. (A) macrophage phenotypical changes in response to (A1) nanotopographies identified by (A2) nanoarray-enabled high-throughput screening through mechanotransduction and (A3) epigenetic modulation. (B) Nanotopography arrays generated using dynamic laser interference lithography (DLIL). Two coherent beams with a variable angle of incident (η') resulted from the curved interferometer creating interference fringes with spatially changing width (Λ) on (B1) a photoactive polymer-coated surface, and DLIL generated over 100,000,000 topographies with varying sizes and shapes including micro/nanolines, micro/nanogrids, and hierarchical structures on a single chip, described as (B2) a nanotopography array. The image of the hologram resulting from nanostructure reflections under ambient light was acquired by using a mobile device camera. The pseudocolored optical microscope image (B2, left) represents the nanotopography array, and the topography starting point was set to be the origin in describing positions on the substrate (i.e., the top-left quadrant contains no topography). Pseudocolored SEM images (B2, right) showed representative topographies across the array. (C) Illustrations of systematic mapping of macrophage phenotypical responses (left) and machine-learning-based predictions and identified hotspots (right). (D) Investigating mechanisms of nanotopography-mediated epigenetic changes and inflammatory responses using hotspot scaled-up nanotopography patterns.

to face substantial obstacles. The challenges posed by inflammatory responses, fibrotic encapsulation, and host rejection reflect the complexity of successfully integrating biomedical implants into clinical practice and the need for continued research to overcome these obstacles. For instance, the clinical application of combined anti-inflammatory drug delivery has been adopted;[13,14] however, this approach usually offers only a short-term solution, with effectiveness lasting typically up to a month. One approach to prolong drug release has been to chemically modify the drug formulation or carrier coating,[15−18] but this has only proven to be an incremental improvement. Yet, sustained immune system suppression has significant limitations, such as increased risks of infections, malignancies, autoimmune complications, and drug resistance. In an alternative approach, integrating biophysical cues onto the interfaces of biomedical implants presents a promising strategy for modulating the behavior of inflammatory cells.[19−21] This regulation is achieved through mechanisms such as clustering of integrins,[22] remodeling of the cytoskeleton,[23] mechanotransduction,[24,25] and modulation of epigenetic factors.[26,27] Importantly, these methods facilitate the control of inflammatory responses in a mechanical manner that is specifically localized to the surface of the implant. This targeted approach is highly beneficial as it avoids the potential drawbacks associated with the widespread suppression of immune responses.[28] By specifically targeting the modulation of inflammatory responses to the immediate vicinity of the implant, this localized strategy ensured that natural immunological functions are preserved globally and improved the compatibility and successful integration of biomedical implants in clinical applications.[29]

Macrophages, being the first line of defense against pathogens, play a pivotal role in regulating innate immunity and tissue repair and regeneration processes, with their specific functions determined by their activation state and phenotypic profile. Recent studies have revealed that macrophages exhibit dynamic phenotypic plasticity, which is crucial in regulating both inflammatory responses and tissue regeneration.[30,31] It can transition between the classically activated proinflammatory state (M1) and the alternatively activated anti-inflammatory state (M2) with a plethora of intermediate phases composing a phenotypic spectrum that is dictated by environmental signals.[32] As the most abundant cell type recruited to the biomedical interface following implantation, the phenotypic state of macrophages influences the inflammatory state and directly dictates whether the implant will undergo tissue integration or fibrous encapsulation.[9,33,34] Despite the growing awareness and emphasis recent studies

https://doi.org/10.1021/acsnano.4c04406
ACS Nano 2024, 18, 25465−25477

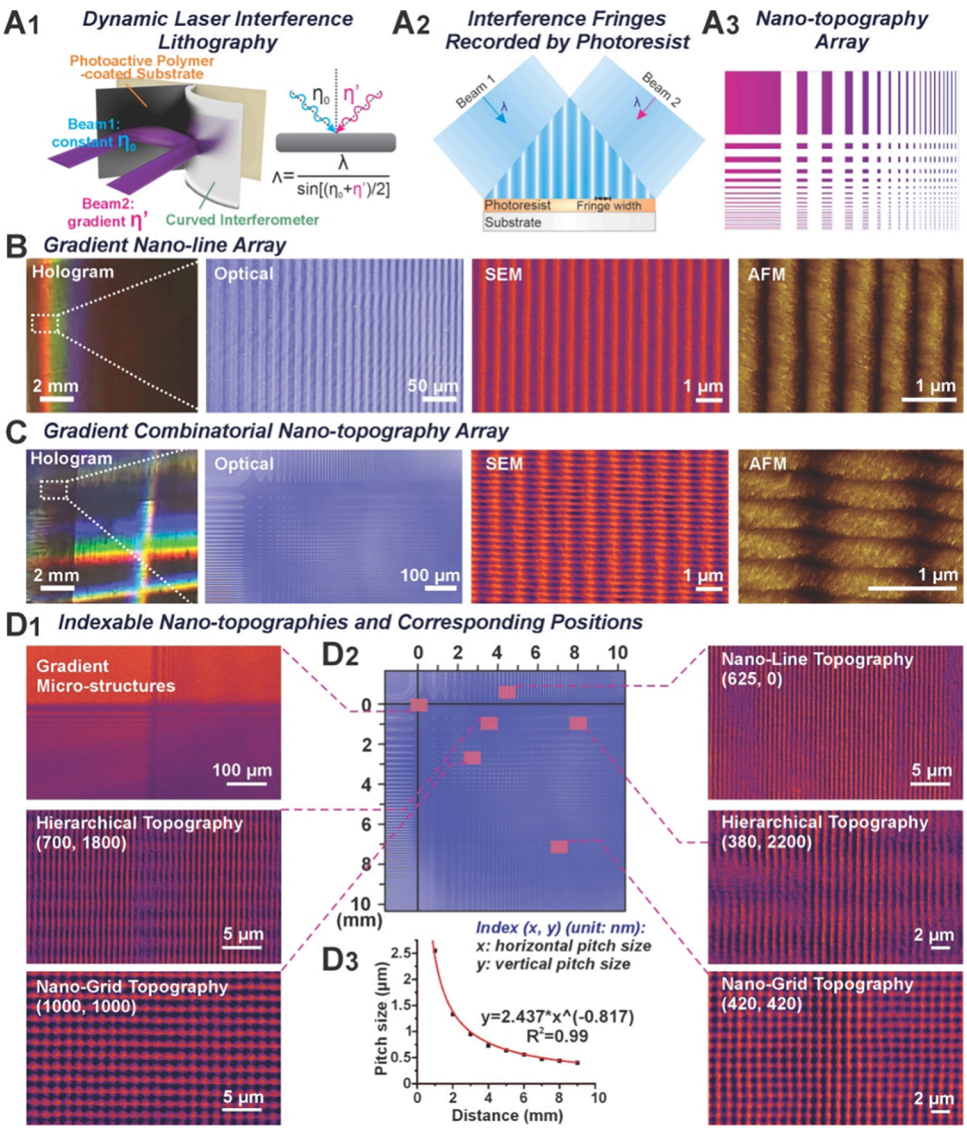

Figure 2. Tunable combinatorial nanotopography arrays with diverse micro/nanostructures generated by dynamic laser interference lithography (DLIL). (A) Schematic diagram illustrating (A1, A2) the working principle of DLIL, resulting in (A3) nanotopography array. A collimated beam generated from a 325 nm helium−cadmium (He−Cd) laser irradiates on a curved interferometer, and the reflected laser interferes with the coherent beam directly irradiated on (A1) the surface of the substrate. (A2) The interference fringes are recorded by cross-linking a photoreactive polymer, photoresist layer, and (A3) result in a spatially changing nanotopography array on the surface of the substrate. (B) A representative collection of optical (pseudocolored), SEM (pseudocolored), and AFM images on different regions of the gradient nanoline array generated from a single laser exposure of DLIL. Leftmost image (acquired using mobile device camera) illustrating one-dimensional holographic properties indicative of gradient nanotopographical features. (C) A representative collection of optical (pseudocolored), SEM (pseudocolored), and AFM images on different regions of the gradient combinatorial nanotopography array generated from double laser exposure of DLIL. Leftmost image (acquired using mobile device camera) illustrating two-dimensional holographic properties indicative of gradient nanotopographical features. (D) Indexable nanotopographies and the identification of their corresponding positions on the substrate. (D1) SEM images were taken from various spots across the nanotopography array , and (D2) the camera positions representing their corresponding locations on the substrate were also recorded and (D3) plotted into a fitting curve to reveal the correlation of nanotopography sizes and spatial locations. Nanotopographies were indexed using the average pitch size of 10 continuous fringes at the horizontal and vertical directions, separately. In the correlation graph, the *x*-axis indicates the distance from the nanostructure to the horizontal (or vertical) origin on the substrate, while the *y*-axis indicates the localized average pitch size in the horizontal (or vertical) direction. Curve fitting was carried out using OriginPro 2019.

have placed on utilizing biophysical cues to regulate macrophages-mediated inflammation,[35−39] there are still pivotal challenges that remain unresolved. Specifically, systemic screening and analysis of nanobio interfaces remain elusive due to the complex, plastic, and dynamic nature of macrophage activation. While great efforts were made to create a wide variety of topographies,[21,40−44] limited success has been achieved in generating a comprehensive library to fully represent the varied size and complexity found in natural extracellular matrix (ECM) microenvironments.[45,46] Furthermore, our understanding of the complex mechanotransduction and epigenetic pathways involved is hindered by several constraints. These include the challenges in precisely controlling structure dimensions, the limited diversity in

https://doi.org/10.1021/acsnano.4c04406
ACS Nano 2024, 18, 25465−25477

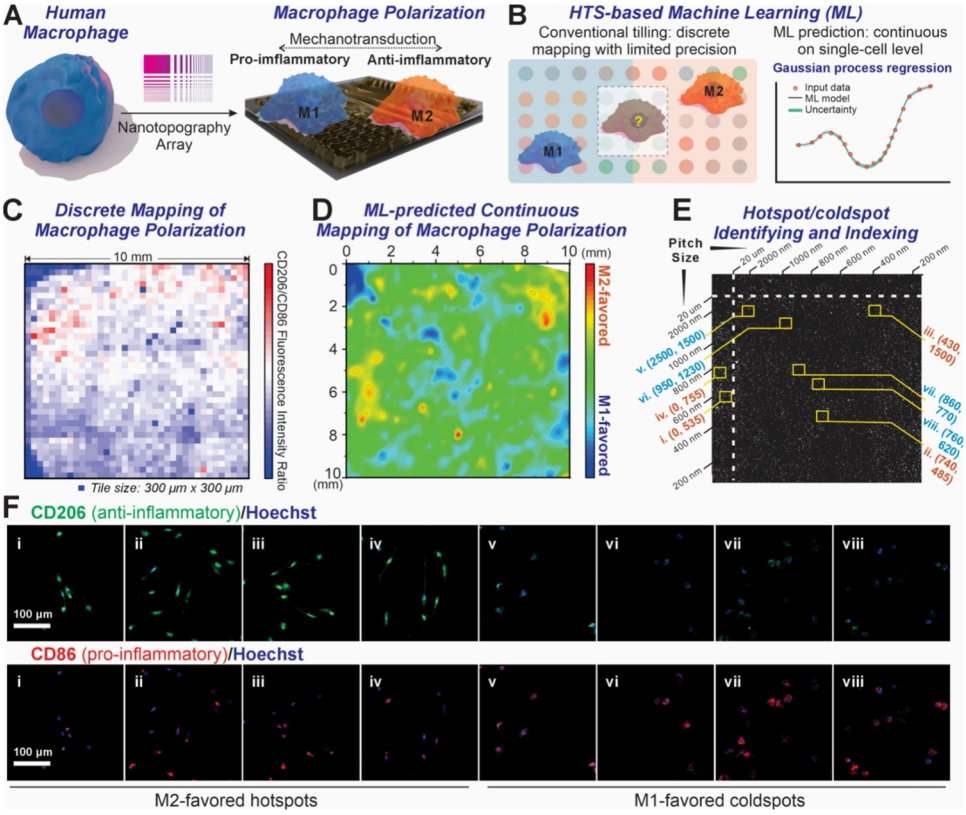

Figure 3. Assessing topography-induced macrophage polarization on nanotopography array through HTS and machine learning (ML). (A) Schematic diagrams showing the process of nanotopography array-based macrophage polarization assay investigating biophysical cue-induced macrophage inflammatory responses. (B) Illustration of HTS and ML methodologies in analyzing macrophage cellular behaviors. (B, left) The conventional tilling−analyzing−stitching approach evaluates averaged signals in tiled small areas, which can be stitched together to represent an overall trend in a larger area. However, since cells were not seeded in full confluency, it limited the minimum tile size due to a lack of signal where cells were absent, hence, limiting the resolution and precision of the generated discrete map. (B, right) The Gaussian process regression ML approach can fill in the blanks by making predictions based on the learned data, hence decreasing the tile size to a single-cell level to obtain a continuous prediction map. (C) Discrete mapping of macrophage polarization characterized by the average fluorescent intensity ratio of CD206 and CD86 antibodies in immunocytochemistry with a tile size of 300 × 300 μm. Edges of the substrate were excluded due to the irregularity. (D) Continuous mapping of macrophage polarization generated from ML predictions. Predictions were made with a step size of 20 μm. (E) Assessment and identification of (i−iv, in red) M2-favored hotspots and (v−viii, in blue) M1-favored coldspots. Hotspot/coldspot indexes and pitch size labels were calculated based on their relative positions on the substrate. (F) Immunocytochemistry images of macrophages seeded around the (i−iv) selected hotspots and (v−viii) coldspots. Scale bars are identical across the images in panel (F).

available geometries, and the lack of broad applicability across different platforms incorporating nanostructures. These constraints also limit the effective integration of this knowledge into the design of nanobio interfaces for biomedical implants, thereby affecting their potential success in medical treatments.

To address the aforementioned challenges, we devised a combinatorial biophysical cue (CBC) array-based strategy. This strategy is specifically designed for high throughput screening (HTS) and analysis of nanobio interfaces, focusing on the epigenetic modulation of macrophages (Figure 1A). Our CBC array can generate over 100,000,000 topographies with various geometries, including lines, grids, and hierarchical patterns and sizes ranging from 200 nm to tens of micrometers, which demonstrate one of the most comprehensive arrays for screening macrophage polarization in a high throughput manner (Figure 1B). Moreover, we also demonstrated the versatility of this approach as it may be extended to various substrates, such as medical grade (5) titanium sheets that are commonly utilized in biomedical implants. The diverse array of topographical features allows us to screen and analyze the heterogeneous responses of macrophages to the bionano interface in a high-throughput manner. Moreover, the integration of high-throughput data processing and machine-learning (ML) techniques enabled the generation of systematic structure−function maps, elucidating the influence of topography on macrophage polarization. These maps were then used to identify nanobio interfaces optimized for macrophage mechanotransduction and epigenetic modulation pathway research (Figure 1C,D). More importantly, the identified topographies can be reproduced in model biomedical implant devices commonly seen in bone grafts for potential inflammatory response suppression and tissue integration promotion in clinical applications. In this work, we integrated advanced nanofabrication, high-throughput screening, and machine learning to establish a promising platform for optimizing and investigating complex nanostructure-regulated inflammatory responses and the associated epigenetic pathways in macrophages.

RESULTS

Generating Combinatorial Biophysical Cue Arrays Using Dynamic Interference Lithography. First, we

https://doi.org/10.1021/acsnano.4c04406
ACS Nano 2024, 18, 25465−25477

sought a high throughput fabrication technique to create combinatory arrays to screen macrophage polarization. Recently, we pioneered a dynamic laser interference lithography (DLIL) technique enabling rapid large-scale generation of "nanoarray-on-a-chip", which holds immense promise in HTS-based analysis and potential for transferable biomedical applications.[47,48] A conventional laser interference lithography (LIL) technique generates large-scale homogeneous line, grid, or dot-patterned nanoarrays with fixed sizes on photoactive polymer (photoresist, PR)-coated substrates by using a flat interferometer (Lloyd's mirror) to split coherent beams and create periodic interference patterns with fixed spatial angle[49,50](Figure S1). Building upon this, we further developed DLIL, which uses a curved interferometer to generate continuously varying spatial angles between the two coherent beams (Figure 2A). Through this optical design, DLIL generated gradient line arrays that imparted more than 10,000 micro- and nanolines on the surface of the substrate with gradually changing sizes ranging from 20 μm to 200 nm in one single laser exposure event with the smallest possible feature size around 200 nm (Figure 2B). By further rotating the exposed substrate for 90° and performing a second DLIL exposure, a combinatorial 2D array containing around 100,000,000 micro- and nanostructures with varying shapes (i.e., lines, grids, and hierarchical patterns) can be fabricated in a few seconds (Figure 2C). The fabricated nanostructures were proven to possess high precision, reproducibility, and, most significantly, indexing ability. By examining the shapes and sizes of nanostructures from various locations on the fabricated array by using scanning electron microscopy, we established a precise formula that relates the sizes of the nanostructures to their corresponding positions (Figure 2D). Nanostructures were indexed as (x, y) where x and y (unit: μm) indicate the micro/nanostructure sizes at the x and y direction, and the corresponding positions were described as the distance to the first fringe along the x- and y-axis. This one-to-one correspondence between the nanostructure and its position on the fabricated CBC array made it possible to analyze the HTS cell assays later and track them back to identify hotspot topographies. In parallel, cell viability tests on PR-coated substrates ensured the biocompatibility of the cross-linked photoreactive polymers used in LIL and DLIL (Figure S2). Furthermore, to ensure the DLIL-based screening strategy could eventually translate into the study and optimization of biomedical implants and devices, we tested and confirmed the formation of both CBC arrays and homogeneous patterns on prime-grade silicon and implant-grade titanium alloys (GR5 Ti-6Al-4 V)[51] as a proof of concept (Figure S3). The coatings on silicon and titanium chips were found to be homogeneous, biocompatible, and chemically inert, providing great promise in translational research. By employing the DLIL technique, we successfully demonstrated the rapid, maskless, and high-throughput generation of large-scale combinatorial arrays comprising a wide range of micro- and nanostructured biophysical cues. Notably, this is the first demonstration where such combinatorial nanoarrays have been created on silicon chips and titanium alloys, widely used materials in clinical applications. Furthermore, it is important to note that stiffness and the nanotopographies highlighted in the current article play a crucial role in biophysical cues. Therefore, we have furthered demonstrate the capability of our platform to modulate the stiffness of the nanopatterns (Figure S4). Collectively, our findings validate the versatility of this approach in generating intricate topographical landscapes for studying the influence of biophysical cues on cellular responses.

High-Throughput Screening and Machine-Learning-Based Prediction of Nanotopography-Regulated Inflammatory Responses. We then performed HTS inflammatory assays on the CBC arrays. In this study, we utilized the THP-1 human monocyte cell line to evaluate the topography-induced inflammatory response, as it has been established as a reliable model for studying monocyte-macrophage functions, mechanisms, signaling pathways, and modulations of monocyte and macrophage activities. THP-1 monocytes were differentiated into adherent resting (M0) macrophages and were allowed to interact with the CBC arrays for 48 h (Figure 3A). To analyze their inflammatory responses, macrophages were fixed and dual-stained with representative M1 markers CD86 and CD206 through immunohistochemistry. Fluorescence images were taken across the substrate in 300 × 300 μm increments. To generate a comprehensive overview of macrophage−nanotopography interactions across the entire CBC array substrate, a total of 1600 individual images were stitched together, excluding the edge regions due to potential systematic errors. We measured and analyzed the average fluorescent intensity ratio of CD206 and CD86 in each 300 × 300 μm image to characterize macrophage polarization profiles. A high CD206/CD86 ratio would indicate that macrophages interacted with the corresponding topography and polarized toward an M2-like phenotype. Conversely, a low CD206/CD86 ratio suggested that the corresponding topography favored an M1 phenotype. The heatmap of the CD206/CD86 ratio (Figure 3C) showed general trends of M1-like polarization (blue) and M2-like polarization (red) induced in different areas of the CBC arrays. However, a large volume of data is lost when generalizations are made regarding large numbers of cells by averaging their behavior. This is further exacerbated by the fact that within a 300 × 300 μm image, there are thousands of topological units that are treated as average behavior. Moreover, this averaging process does not adequately address abnormal data points, including outliers, background-induced systematic errors, and random errors. Such factors can significantly influence the average fluorescence intensity, thereby compromising the reliability of the findings. To more precisely characterize the macrophage−nanotopography interactions, we used a semiautomatic data processing approach to create cell masks and measure CD206/CD86 ratio for each individual cell (Figure S5) and further incorporated a Gaussian Process Regression (GPR)-based ML algorithm to analyze, predict, and describe macrophage−nanotopography interactions with a step size of 20 μm (typical size of a macrophage) and generated a consecutive inflammatory map (Figure 3D). The GPR machine-learning approach, which is a widely tested and optimized probabilistic model, was utilized for the analysis. This model specializes in predicting unknown results based on isolated data points, and its main purpose was to prevent interference from areas where no cells exist. Using this ML-based approach, we not only filled the blanks between discretized experimental data with over 200,000 predictions (Figure S6) but also instructed and screened out the false-positive outliners in the discretized maps (Figure 3B). From the generated inflammatory map, M1-like polarization was shown to be dominant in the top left corner of the CBC array, where no nanostructure exists, suggesting a significant possibility of chronic inflammatory response from

https://doi.org/10.1021/acsnano.4c04406
ACS Nano 2024, 18, 25465−25477

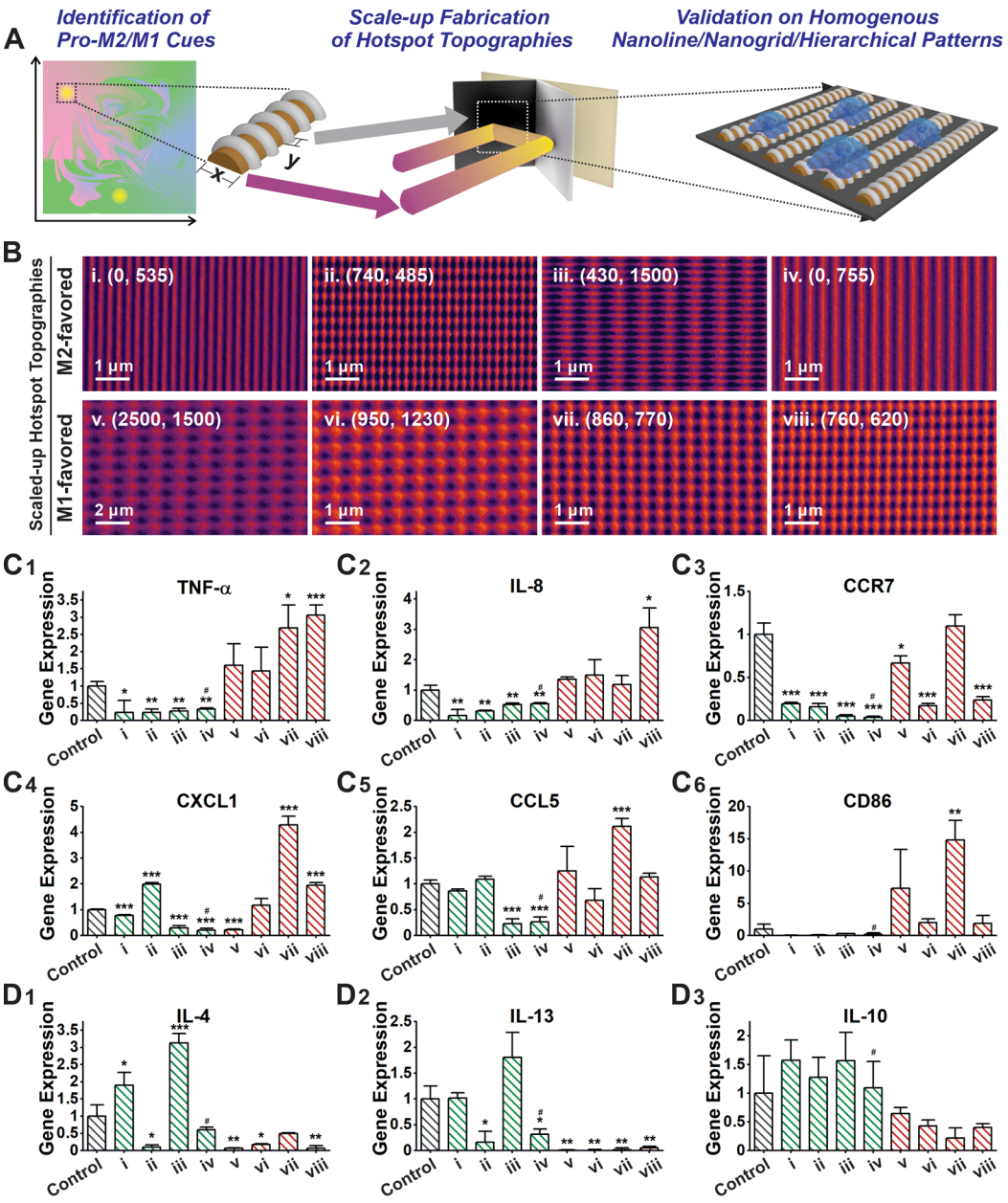

Figure 4. Scaled-up hotspot/coldspot nanopatterns demonstrating topography-induced macrophage inflammatory response regulations. (A) Schematic diagrams showing the scale-up synthesis of nanopatterns containing uniform hotspot/coldspot topographies using LIL. (B) Pseudocolored SEM images of homogeneous nanopatterns matching hotspot/coldspot topographies, individually. Nanopatterns were labeled with hotspot/coldspot indexes, their exact measures are summarized in Table S1. (C, D) The scaled-up nanopatterns induce macrophage polarization and inflammatory responses based on RT-qPCR analysis. (i–iv, green) M2-favored topographies and (v–viii, red) M1-favored topographies generally showed opposite trends in regulating proinflammatory gene expressions (C1–C6) and anti-inflammatory gene expressions (D1–D3) compared to the plain substrate with no nanotopography as a negative control (control, gray). Data are shown as mean ± stdev. $n = 3$ experimental replicates. Statistical analysis by student's unpaired t test. The control group refers to the polymer-coated glass substrate without any nanotopography. *$P < 0.05$, **$P < 0.01$, ***$P < 0.001$, $n = 3$, comparison was preformed between the marked group and the control group. #$P < 0.05$, comparison performed between the proinflammatory (860, 770) and anti-inflammatory (0, 755) nanopatterns.

activated macrophages in the absence of immune-regulating nanotopographies. Among the nanopatterns, grid patterns (shown in the diagonal range where x and y are in close approximation) clearly favor the M1-like polarization with many coldspots of CD206/CD86 ratio. Please note that the colocalization of CD86 and CD206 staining may suggest the existence of an M1/M2 transition state in the macrophages. Although there is no overall trend in the distribution of M2 polarization within the CBC array, line patterns and hierarchical patterns located close to the edges of the map seem to have a positive effect on M2 polarization. Interestingly, the polymer substrate without any nanopattern was found to have a pro-M1 polarization effect (Figure S7). To further examine the topographical-regulating effect on macrophage polarization, four M2-favored hotspots with nanoline or hierarchical structures [indexed by their topographies as i. (0, 535), ii. (740, 485), iii. (430, 1500), and iv. (0, 755)] and four M1-favored coldspots with nanogrid structures [v. (2500,

https://doi.org/10.1021/acsnano.4c04406
ACS Nano 2024, 18, 25465–25477

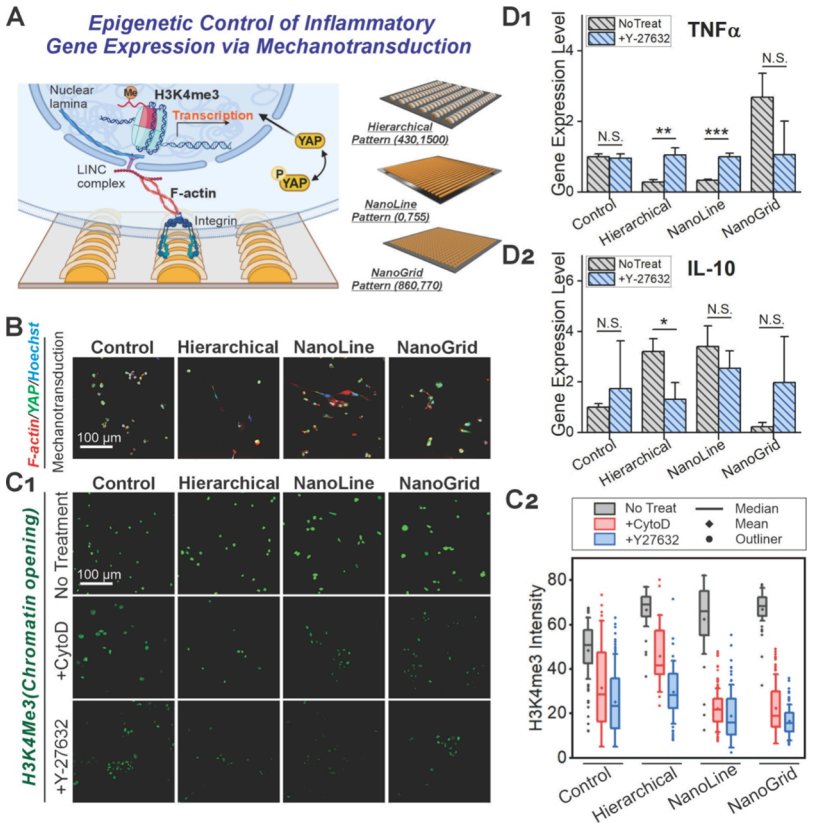

Figure 5. Nanotopographies induce macrophage polarization via mechanotransduction and cooperative epigenetic modulation. (A) Proposed mechanism and key pathway markers on topography-induced macrophage inflammatory responses. The schematic diagram showing the hierarchical pattern to cover the diverse types of nanotopographies that could influence the polarization of macrophages. (B) Immunofluorescence staining of YAP and phalloidin staining of cytoskeleton F-actin showing macrophage morphology changes and YAP translocation associated with representative hierarchical, nanogrid, and nanoline topographies. Scale bars are identical across the images within panel (B). (C) (C1) Immunofluorescence images and (C2) quantifications of epigenetic activity marker H3K4me3 in no treatment, + CytoD, and + Y-27632 conditions. Scale bars are identical across the images within panel (C1). $n > 40$. (D) RT-qPCR accessing ROCK-dependent topography-regulated expression of (D1) proinflammatory and anti-inflammatory genes. Data are shown as mean ± stdev. $n = 3$ experimental replicates. Statistical analysis by student's unpaired t test. N.S.= not significant, $*p < 0.05$, $**p < 0.01$, $***p < 0.001$.

1500), vi. (950, 1230), vii. (860, 770), and viii. (760, 620)] were selected, and corresponding nanostructures were easily obtained based on the previously mentioned position-nanostructure-corresponding formula (Figure 3E,F).

Scaling Up and Confirming the Accuracy of Predicted Nanotopographies. Next, we validated whether the predicted hot-spot and cold-spot nanostructures represent effective inflammatory-regulating topographies. First, we scaled up the eight selected hotspot/coldspots using conventional LIL (Figure 4A). Rotation stage angles for synthesizing each homogeneous nanopattern were calculated using the equation: $\Lambda = \lambda / \sin \theta$, where Λ is referred to as the pattern period or periodic pitch size, λ corresponds to the laser wavelength (325 nm), and θ as the angle of incident. Overall, eight selected nanotopography patterns were fabricated separately. LIL parameters are summarized in Table S1, and shapes and sizes of the scaled-up nanotopographies were also confirmed by scanning electron microscope (Figure 4B) and atomic force microscopy (Figure S8). We then seeded macrophages and repeated the inflammatory assay using procedures identical with those described in the mapping experiment. The expression of inflammatory genes and proteins was analyzed across all eight scaled-up substrates containing nanotopographical features as well as a negative control substrate without nanotopography, using immunocytochemistry and reverse transcription-quantitative polymerase chain reaction (RT-qPCR) techniques, respectively. First, in the immunocytochemistry assay, the trend of M1 (CD86) and M2 (CD206) biomarker expression accurately reflected the predicted results in the inflammatory map (Figures S9 and S10). For example, the predicted M2-favored topographies i, ii, iii, and iv showed significantly (3.62, 3.09, 2.64, and 4.12-fold, respectively) higher CD206/CD86 ratios compared to the negative control, directly validating the mapping result. However, the experimental CD206/CD86 ratios do not match the predicted numbers exactly, which could be due to the cytokine-signaling and cell−cell interaction among the macrophage population on the same substrate.[52−54] Cells cultured on the CBC array exhibited heterogeneous phenotypes and inflammatory responses due to the high diversity of nanotopographical features, whereas cells interacting with the scaled-up topographies displayed relatively uniform responses owing to the homogeneous biophysical cues. F-actin stained by phalloidin also revealed cytoskeleton and morphology changes of macrophages when reacting with different topographies (Figure S11). The spindle-shaped elongated cell bodies and cytoplasmic extensions on the apical ends of the cell bodies suggest M2-like morphologies were found to be dominant on nanostructures (i), (ii), (iii), and (iv); on the contrary, the majority of cells showed M1-like enlarged amoeboid cellular

https://doi.org/10.1021/acsnano.4c04406
ACS Nano 2024, 18, 25465−25477

morphologies with more spread-out and flat bodies on nanostructures (v), (vi), (vii), and (viii). Similarly, RT-qPCR results indicated that the robust inflammation suppression effect of predicted M2-favored nanostructures i, ii, iii, and iv by the 0.231-, 0.235-, 0.279-, and 0.332-fold, respectively, decrease in TNFα expression compared to the plain surface. Moreover, through a preliminary transcriptomic study, our results show the significant differences and high enrichment factors on inflammation-related pathways. Furthermore, our analysis also revealed significant alterations in focal adhesion and cell-membrane-receptor-related pathways across different nanopatterns. These findings further support the potential for surface-mediated modulation of macrophage polarization (Figures S12 and S13).

The prediction of M2-favored nanostructure is further supported by the downregulation of various proinflammatory genes (IL-8, CCR7, CXCL1, CCL5, and CD86) (Figure 4C), as well as the upregulation of anti-inflammatory genes (IL-4, IL-13, and IL-10) (Figure 4D). M1-favored nanostructures (v–viii) showed the opposite inflammatory regulating effect and further confirmed their inflammation-promoting function as predicted. Indeed, there are occasional inconsistencies, but the general trend clearly supports the overall prediction of the inflammatory map. By effectively utilizing LIL techniques, we successfully achieved precise control over generating nanostructures that either suppress inflammation or promote inflammation. This enabled the successful scaling up of these distinct nanostructured surfaces. Moreover, we further validated the accuracy and reliability of our findings by confirming the inflammatory responses mapped on the CBC array platform. Collectively, our results show the versatility of this approach in fabricating and screening intricate nanotopographical cues to modulate cellular inflammatory states, paving the way for the rational design of biomedical implants with improved integration and functional outcomes.

Epigenetic Changes Associated with Macrophage Polarization. Last, we sought possible mechanisms associated with nanotopography-regulated macrophage polarization. Several excellent studies have sequentially revealed key pathways in mechanotransduction, such as tension-induced actin polymerization,[38] Hippo signaling inhibition,[55] YAP/TAZ translocation,[25,56,57] and epigenetic modification.[28,58,59] However, how different nanotopographies regulate mechanotransduction and macrophage polarization remains largely unexplored. Understanding the mechanisms behind regulating inflammatory response by nanotopography is crucial for developing therapeutic biomaterials and mitigating side effects associated with biomedical implants (Figure 5A). To fill this gap, we selected the inflammation-suppressing hierarchical (430, 1500) and nanoline (0, 755) topographies, inflammation-promoting nanogrid topography (860, 770), and negative control with no nanotopographies for in-depth mechanism studies. We first stained F-actin using dye-labeled phalloidin (Figure 5B). Despite the observed cytoskeleton arrangement and macrophage morphology change, F-actin expression level differences were found to be insignificant. We also analyzed YAP1 expression by using immunocytochemistry. YAP/TAZ control cell growth, proliferation, and apoptosis in response to mechanical tension and are negatively regulated by phosphorylation from downstream Hippo activation. From our observations, macrophages cultured on nanoline and hierarchical topographies exhibited higher percentages of YAP-nucleus colocalization, suggesting a higher level of YAP/TAZ translocation from the cytoplasm to the nucleus.

However, due to the significant differences in cell morphology, cell body area, and nucleus area between M1- and M2-like macrophages, further investigation is needed to determine whether the observed differences in colocalization arise from topography-induced mechanical cue transduction and to elucidate the detailed role of YAP/TAZ Hippo signaling in regulating macrophage inflammatory responses. Therefore, we next used trimethylation of histone H3 at lysine 4 (H3K4me3) as a transcriptionally active chromatin marker[60] to study the epigenetic activity in macrophages cultured on the nanotopographies (Figure 5C). Based on the average H3K4me3 intensity in the nucleus of macrophages, slightly higher levels of transcriptional activations were observed in all three nanostructures with 1.38-, 1.38-, and 1.29-fold increases, separately, relative to the negative control, suggesting that all three topographies promoted epigenetic activations, although the specific genes activated may differ. To further investigate the associated pathways of the activated epigenetic regulation, cytochalasin-D (CytoD), an actin polymerization inhibitor, and Y-27632, an Rho-associated protein kinase (ROCK) inhibitor, were added to the macrophages after their initial attachment to the nanotopographies. Transcriptional activities marked by H3K4me3 showed significant levels of suppression in the presence of CytoD and Y-27632 in both nanoline and nanogrid topography. Although less significant, both hierarchical topography and the negative control showed similar transcriptional suppression effects for CytoD and Y-27632. This evidence further supported that epigenetic modulations may be a possible mechanism for nanotopography-mediated macrophage polarization.

Furthermore, RT-qPCR was used to examine the effect of ROCK-inhibitor Y-27632 on macrophage inflammatory responses (Figure 5D). In the absence of Y-27632, TNFα expression was downregulated on hierarchical and nanoline topographies and upregulated on nanogrid topographies, as expected. However, in the presence of Y-27632, plain substrates exhibited no change in TNFα expression. Interestingly, the up-/downregulating effects of the three nanotopographical surfaces were completely inhibited, resulting in uniform TNFα expression levels across all groups. The expressions of the anti-inflammatory marker IL-10 also showed a similar inhibiting effect, despite being less significant. The significant nullifying effect of Y-27632 on the inflammatory-regulating effects of nanotopography strongly suggests a heavy reliance on the ROCK signaling pathway for this regulation mechanism. While the exact mechanism behind the nanotopography-induced epigenetic changes and inflammatory responses still needs more research, it is evident that topographical cues control the polarization of macrophages via mechanotransduction-mediated pathways and the activation of ROCK-dependent epigenetics.

CONCLUSIONS

In summary, our study highlights the pivotal role that surface nanostructures play in modulating inflammation within biomedical implants. Until now, the field has faced a substantial gap in the availability of effective methodologies for the systematic screening and nuanced analysis of complex nanobio interfaces. Leveraging the DLIL technique, we established one of the most extensive combinatorial nanoarrays to date. Utilizing an array of over a hundred million diverse

https://doi.org/10.1021/acsnano.4c04406
ACS Nano 2024, 18, 25465–25477

topographies allows for a comprehensive examination of the relationship between nanotopography and macrophage polarization. The topographies included in this range vary from basic lines and grids to intricate hierarchical structures, covering a wide size spectrum, ranging approximately from 200 nm to over 20 μm. This wide range of sizes mirrors the complex and intricate nature of natural ECM.

We also successfully generated an inflammatory map by integrating HTS and ML. This map enables the precise prediction of nanotopographies that induce M2-like and M1-like macrophage responses. These predictions were subsequently confirmed through experiments on nanotopography substrates fabricated on a larger scale. Initial mechanistic investigations point toward mechanotransduction-associated epigenetic activation as a key pathway. Additionally, signaling pathways such as Hippo YAP/TAZ and ROCK signaling are suggested to play significant roles in macrophage polarization induced by topographical cues. The capability of our CBC array to screen a vast diversity of nanostructures and predict cellular behavior "hotspots" using machine-learning positions it as an unparalleled platform. It facilitates the comprehensive optimization and exploration of coating nanostructures on therapeutic biomaterials and biomedical implants. This approach not only deepens our comprehension of nanobio interactions but also unlocks the potential for creating next-generation biomaterials designed to precisely modulate immune responses, ultimately leading to enhanced therapeutic outcomes.

Moving forward, a critical step would be the in vivo validation of the nanostructures predicted for biomedical implants. While our fabrication techniques allow for depth of focus adjustments on the order of millimeters, they are primarily suited for implants with smooth surfaces. This specificity arises because irregular surfaces may distort the interference pattern, potentially limiting the applicability of our methods. Despite this, the utilization of the CBC array and machine learning for HTS of nanobio interfaces has proven to be a valuable tool in exploring the guidance of macrophage polarization and inflammation through biophysical cues. Drawing definitive conclusions about epigenetic activation as the principal mechanism requires further validation, potentially through advanced methodologies such as assay for transposase-accessible chromatin using sequencing (ATAC-seq). Similarly, the specific contributions of YAP/TAZ signaling and ROCK signaling to inflammatory responses demand deeper investigation, possibly through single-cell RNA sequencing (scRNA-seq). By refining the machine-learning model, conducting thorough mechanistic studies, and assessing the clinical application viability, the CBC array-based approach promises to unlock its full potential. This development could significantly enhance the design of nanostructured coatings for therapeutic biomaterials and biomedical implants, ushering in a new era of precisely engineered solutions for healthcare challenges. Finally, considering the significant disparities between in vitro and in vivo inflammatory responses to nanotopographies, it is crucial to extend our research using animal models. Future studies should utilize the CBC array to screen and investigate the responses of macrophages to diverse nanotopographies in vivo.

METHODS

Nanotopography Array Fabrication Using Dynamic Laser Interference Lithography (DLIL). Glass slides (MSE Supplies), grade 5 titanium plate (TC4/GR5 Ti-6Al-4 V, LTKJ), and silicon wafers (MSE Supplies) were cut into individual square pieces with dimensions of 1.2 × 1.2 and 2.5 × 2.5 cm. Substrates were cleaned by sonicating in 1% Triton X-100 (Sigma-Aldrich #X100) aqueous solution, 200 proof ethanol, and Milli-Q ultrapure water, 20 min each. Once the substrates were cleaned, they underwent a drying process in a vacuum. This was followed by an oxygen plasma treatment using the CUTE-MP plasma cleaner from FEMTO SCIENCE. The purpose of this treatment was to further clean and activate the surface, thereby enhancing the adhesion characteristics. To improve photoresist adhesion, Glass and Si substrates were then treated with hexamethyldisilazane (HMDS, Sigma-Aldrich no. 379212) using chemical vapor deposition at 80 °C overnight. The UV-cross-linkable AZ nLOF2020 photoresist (PR, EMD Performance Materials #17998823157; 6:4 dilution using AZ EBR solvent, EMD) was spin-coated on substrates at 6000 rpm for 40 s (WS-650MZ-23NPP spin coater, Laurell technologies), followed by soft bake at 105 °C for 1 min. The DLIL system was composed of a UV laser (IK Series He−Cd 325 nm laser, KIMMON KOHA Laser Systems), a shutter controller (THORLABS), two focusing lenses, one spatial filter with pinhole and collimating lenses, and a rotation stage with a perpendicular curved interferometer. Substrates were secured on the rotation stage and exposed to a UV laser for 15 s at a power density of 0.5 mW/cm^2. Stage angle was kept at 72°. After the first laser exposure, substrates were rotated by 90°, followed by a second laser exposure event. Postexposure bake was carried at 120 °C for 1 min, followed by development in AZ300 MIF Developer (EMD Performance Materials # 18441123163) for 15−25 s and washed in DIW twice. The hologram appeared after drying by flowing N_2 gas. In order to prevent any alterations in surface topographies, the fabricated substrates can be safely stored at room temperature without exposure to light for several months.

Fabrication of Scaled-Up Hotspot/Coldspot Nanopatterns Using Laser Interference Lithography. The preparatory steps for the DLIL process, such as substrate cleaning, oxygen plasma treatment, HMDS coating, photoresist spin-coating, and soft baking, follow the same procedures as those previously mentioned. However, the curved interferometer setup has been replaced with a Lloyd's mirror configuration. The stage angle settings for fabricating each scaled-up topography are summarized in Table S1. Periodic nanoline patterns were generated after a single laser exposure. To create periodic nanogrid or hierarchical patterns, the substrate was rotated 90° following the first laser exposure. The stage angle was then adjusted accordingly, and a second laser exposure was performed. Postexposure baking, developing, and drying procedures followed the same steps as those in the DLIL process.

Characterization of Nanotopography Arrays. Optical images of the nanotopography arrays were taken using a Bio-Rad ZOE Fluorescent Cell Imager. The micro- and nanoscale structures on the substrate surfaces were characterized using a Zeiss Sigma Field Emission Scanning Electron Microscope (FESEM) operated at 20 kV and an atomic force microscope (AFM) from Park Systems (NX10 series) in tapping mode.

Cell Culture. Human leukemia monocytic cell line THP-1 (ATCC) cells were used throughout the experiments. THP-1 monocytes were maintained and proliferated in RPMI Medium 1640 (Gibco #11875−093) supplemented with 10% fetal bovine serum (FBS, Thermo Scientific #A3160502), 1% penicillin−streptomycin (Thermo Scientific #15140148), and 55 μM 2-mercaptoethanol (BME, Gibco #21985_023). To induce differentiation of nonadherent THP-1 monocytes into adherent M0 macrophages, cells were seeded on sterilized nanotopography substrates in the presence of 50 ng/mL phorbol 12-myristate 13-acetate (PMA, Tocris #1201) for 24 h.

Macrophage Polarization on Nanotopography Arrays. All substrates with nanotopographies fabricated using LIL or DLIL were sterilized under UV light in cell culture hoods for 30 min before transferring into cell culture plates. THP-1 monocytes were seeded into individual wells at a cell density of 50,000 cells/cm^2 and differentiated into M0 macrophages for 24 h. A time period of 48 h

https://doi.org/10.1021/acsnano.4c04406
ACS Nano 2024, 18, 25465−25477

was allocated for the cells to interact with the nanotopography arrays in a complete media without the addition of PMA. Following this period, the cells were subjected to analysis in order to evaluate their inflammatory responses.

Immunocytochemistry. Immunocytochemistry was conducted to study nanotopography-induced macrophage polarization after fixation on the nanotopography arrays. All antibodies used, including their vendors, catalog numbers, and dilutions, are summarized in Table S2. Cells were fixed with 4% formaldehyde solution (Sigma-Aldrich #HT5014) at room temperature for 10 min and washed with PBS. Cells were then permeabilized with 0.3% Triton X-100 in PBS, and nonspecific binding was blocked with 5% normal goat serum (Gibco #16210064) at room temperature for 1 h. Samples were incubated with primary antibody solutions diluted in PBS with 1% bovine serum albumin (BSA, Gibco #15260−037) at 4 °C overnight, washed with PBS three times, and then incubated with appropriate fluorophore-labeled secondary antibodies diluted in PBS with 1% BSA at room temperature for 1 h in the dark. Cells were washed to eliminate nonspecific binding and incubated with DNA labeling dye Hoechst 33342 (Thermo Scientific #62249) before mounting on microscope slides using Fluoromount aqueous mounting medium (Sigma-Aldrich #F4680). In the THP-1 cytoskeleton rearrangement assay, F-actin was stained by Alexa Fluor 633 phalloidin (Invitrogen no. A22284) at room temperature for 60 min and washed with PBS two times, followed by Hoechst staining and mounting. All fluorescence images were gained by a Dragonfly Confocal Microscope (Andor Technology Ltd., Belfast, Northern Ireland).

Flow Cytometry. Cells were trypsinized, washed with PBS, and resuspended in FACS buffer (PBS, 1% BSA). 1 μg/mL of primary antibody CD86 (Novus #NBP2−25208) and CD206 (Novus #NBP1−90020) was diluted in FACS buffer and incubated with single-cell suspension for 30 min at room temperature. The cells were washed three times by centrifugation at 500 g for 5 min and resuspend them in 200 μL of ice cold FACS buffer. Cells were then incubated with secondary antibody solution for 30 min at room temperature in the dark, followed by three washes by centrifugation at 500*g* for 5 min and resuspend them in 200 μL of ice cold FACS buffer. Cells were analyzed using an ADAMII-LS-Fluorescence cell analyzer (Nano-Entek, Korea).

Gaussian Process Regression Machine-Learning Model on Mapped Results. A supervised GPR-ML model was generated in MATLAB R2023a to continuously predict the phenotype of THP-1 cells when subjected to various regions of our substrate. The M1-like and M2-like phenotypes were thoroughly examined in order to take their contributions into account. Subsequently, we decided to combine the *X* and *Y* spatial coordinates, which contain information about the position of the cells, into the observation matrix. Furthermore, the corresponding response vector, which contains the biomarker intensity (also termed the *Z*-coordinate), was used as the labels. After separating the observations from the labels, the hyperparameters were optimized using a Bayesian optimizer to ensure the learning process was updated and modified at each new model evaluation. It has been reported that Bayesian optimizers are proficient at finding a global optimum for an objective function in a minimal number of evaluations when tuning hyperparameters by maximizing an acquisition function that will determine the next value where the model should be evaluated. In our model, we used an expected improvement (EI) criterion for the acquisition function to evaluate regions where the model believed the objection function was low and regions where the uncertainty was high. This was accomplished to address the exploitation versus exploration trade-off many scientists encounter when selecting an optimizer. Hence, it was possible to search local areas within the bounds of the optimizer without overexploiting one area and being trapped at a local minimum. Once the optimizer was established, the data was split into 80% training and 20% validation data to allow for holdout cross-validation to determine the model's predictive accuracy. After the model was generated, the minimum and maximum values of the *X* and *Y* coordinates were identified and placed into a 2-D grid composed of 250,000 elements that spanned the area bounded by the minima and maxima (i.e., predicting a cell every 20 μm along the substrate). Finally, this matrix was provided to the GPR-ML model to predict the corresponding phenotype across the substrate. Loss was calculated by calculating the mean square error (MSE) between the measured and predicted points across the substrate.

Gene Expression Analysis by RT-qPCR. Cells polarized on nanotopography substrates were lysed using TRIzol reagent (Invitrogen #15596018). Total RNA extraction, precipitation, and purification were carried out following a vendor protocol (TRIzol Reagent User Guide Pub. No. MAN0001271 C.0). RNA concentrations and A260/280 ratios were measured using a Nanodrop Lite Spectrophotometer (Thermo Scientific). Reverse transcription was carried out using an Autorisierter Thermocycler (Eppendorf) with an AccuPower CycleScript RT PreMix (BIONEER #K-2044). Quantitative PCR was performed using a StepOnePlus Real-Time PCR System (Applied Biosystems) with an SYBR Green Universal Master Mix (Thermo Scientific #4344463). Sequences of PCR primers (Integrated DNA Technologies) are summarized in Table S3. GAPDH was used as a housekeeping gene. Relative mRNA expression levels were calculated using the ΔΔCt method and normalized to gene expression of the negative control where cells were seeded on substrates with no nanotopography.

mRNA Sequencing. Sequencing libraries were prepared and sequenced on a NovaSeq X Plus Series (PE150) platform from Novogene Co. Ltd. RNA-seq results are read in fasta format after fastp data quality evaluation and filtering. DESeq2 was used to analyze the differentially expressed genes.

ASSOCIATED CONTENT

Supporting Information

The Supporting Information is available free of charge at https://pubs.acs.org/doi/10.1021/acsnano.4c04406.

Summary of LIL stage angle settings; antibodies used in immunocytochemistry experiments; primers used in qPCR experiments; periodic line patterns fabricated by LIL and gradient lines fabricated by DLIL; biocompatibility of photoresist proved by cell viability assay; CBC arrays and homogenous patterns fabricated on various materials; modulation of nanopattern stiffness using the DIL technique; 3D heat map of CD206/CD86 fluorescence intensity; 3D visualization of predictions of CD206/CD86 fluorescence intensity; effects on macrophage polarization from control substrate; scale-up fabricated nanotopographies characterized by atomic force microscopy; immunocytochemistry validating hotspot topography-regulated macrophage polarization; flow cytometry characterization of macrophage polarization; F-actin staining showing topography-induced cytoskeleton changes; transcriptomic analysis on macrophages polarized on nanopatterns; pathway analysis on macrophages polarized on pro- and anti-inflammatory nanopatterns (PDF)

AUTHOR INFORMATION

Corresponding Authors

Letao Yang − *Department of Chemistry and Chemical Biology, Rutgers, The State University of New Jersey, Piscataway, New Jersey 08854, United States; Key Laboratory of Spine and Spinal Cord Injury Repair and Regeneration of Ministry of Education, Department of Orthopedics, Tongji Hospital affiliated to Tongji University, Frontier Science Center for Stem Cell Research, School of Life Science and Technology, Tongji University, Shanghai 200065, China;* orcid.org/0000-0002-0572-9787; Email: yangletao@tongji.edu.cn

https://doi.org/10.1021/acsnano.4c04406
ACS Nano 2024, 18, 25465−25477

Ki-Bum Lee − *Department of Chemistry and Chemical Biology, Rutgers, The State University of New Jersey, Piscataway, New Jersey 08854, United States;* orcid.org/0000-0002-8164-0047; Phone: +1-732-445-2081; Email: kblee@rutgers.edu; Fax: +1-732-445-5312

Authors

Yannan Hou − *Department of Chemistry and Chemical Biology, Rutgers, The State University of New Jersey, Piscataway, New Jersey 08854, United States*

Brandon Conklin − *Department of Chemistry and Chemical Biology, Rutgers, The State University of New Jersey, Piscataway, New Jersey 08854, United States;* orcid.org/0000-0002-6834-3275

Hye Kyu Choi − *Department of Chemistry and Chemical Biology, Rutgers, The State University of New Jersey, Piscataway, New Jersey 08854, United States*

Complete contact information is available at: https://pubs.acs.org/10.1021/acsnano.4c04406

Author Contributions

The manuscript was written through the contributions of all authors. All authors have approved the final version of the manuscript.

Notes

The authors declare no competing financial interest.

ACKNOWLEDGMENTS

K.-B.L. acknowledges the partial financial support from the NSF (CBET-1803517), the New Jersey Commission on Spinal Cord (CSCR17IRG010; CSCR16ERG019), NIH 26 R01 (1R01DC016612, 1R01NS130836-01A1, 3R01DC016612-01S1, and 5R01DC016612-02S1), NIH RM1 (RM1 NS133003-01), NIH R21 (R21 NS132556-01), Alzheimer's Association (AARG-NTF-21-847862), CDMRP (OCRP, OC220235P1), N.J. Commission on Cancer Research (COCR23PPR007), and HealthAdvance (NHLBI, U01HL150852). L.Y. acknowledges the National Natural Science Foundation of China (32301106), the Fundamental Research Funds for the Central Universities (22120240435) and Peak Disciplines (Type IV) of Institutions of Higher Learning in Shanghai. B.C. acknowledges fellowship support from the NIH T32 training program (5T32NS115700-02). Authors sincerely thank Professor Yoon-Seong Kim (Robert Wood Johnson Medical School, Rutgers University) for providing access to the confocal microscope for this study. We appreciate Hyunjun Jang's assistance with AFM characterization. We thank all K.-B.L. group members for providing insight and expertise that greatly assisted the research. The authors acknowledge the use of Biorender to create some figures.

REFERENCES

(1) Finbloom, J. A.; Huynh, C.; Huang, X.; Desai, T. A. Bioinspired nanotopographical design of drug delivery systems. *Nature Reviews Bioengineering* **2023**, *1* (2), 139−152.

(2) Dondossola, E.; Friedl, P. Host responses to implants revealed by intravital microscopy. *Nature Reviews Materials* **2022**, *7* (1), 6−22.

(3) Abhari, R. E.; Izett-Kay, M. L.; Morris, H. L.; Cartwright, R.; Snelling, S. J. B. Host-biomaterial interactions in mesh complications after pelvic floor reconstructive surgery. *Nat. Rev. Urol* **2021**, *18* (12), 725−738.

(4) Zhu, M.; Li, W.; Dong, X.; Yuan, X.; Midgley, A. C.; Chang, H.; Wang, Y.; Wang, H.; Wang, K.; Ma, P. X.; Wang, H.; Kong, D. In vivo engineered extracellular matrix scaffolds with instructive niches for oriented tissue regeneration. *Nat. Commun.* **2019**, *10* (1), 4620.

(5) Santoro, F.; Zhao, W.; Joubert, L. M.; Duan, L.; Schnitker, J.; van de Burgt, Y.; Lou, H. Y.; Liu, B.; Salleo, A.; Cui, L.; Cui, Y.; Cui, B. Revealing the Cell-Material Interface with Nanometer Resolution by Focused Ion Beam/Scanning Electron Microscopy. *ACS Nano* **2017**, *11* (8), 8320−8328.

(6) Jiang, N.; Guo, Z.; Sun, D.; Li, Y.; Yang, Y.; Chen, C.; Zhang, L.; Zhu, S. Promoting Osseointegration of Ti Implants through Micro/Nanoscaled Hierarchical Ti Phosphate/Ti Oxide Hybrid Coating. *ACS Nano* **2018**, *12* (8), 7883−7891.

(7) Xie, S.; Huang, J.; Pereira, A. T.; Xu, L.; Luo, D.; Li, Z. Emerging trends in materials and devices-based electric stimulation therapy for tumors. *BMEMat* **2023**, *1* (3), No. e12038.

(8) Noskovicova, N.; Hinz, B.; Pakshir, P. Implant Fibrosis and the Underappreciated Role of Myofibroblasts in the Foreign Body Reaction. *Cells* **2021**, *10* (7), 1794.

(9) Doloff, J. C.; Ma, M.; Sadraei, A.; Tam, H. H.; Farah, S.; Hollister-Lock, J.; Vegas, A. J.; Veiseh, O.; Quiroz, V. M.; Rakoski, A.; Aresta-DaSilva, S.; Bader, A. R.; Griffin, M.; Weir, G. C.; Brehm, M. A.; Shultz, L. D.; Langer, R.; Greiner, D. L.; Anderson, D. G. Identification of a humanized mouse model for functional testing of immune-mediated biomaterial foreign body response. *Sci. Adv.* **2023**, *9* (24), No. eade9488.

(10) Sridharan, R.; Cameron, A. R.; Kelly, D. J.; Kearney, C. J.; O'Brien, F. J. Biomaterial based modulation of macrophage polarization: a review and suggested design principles. *Mater. Today* **2015**, *18* (6), 313−325.

(11) Davenport Huyer, L.; Pascual-Gil, S.; Wang, Y.; Mandla, S.; Yee, B.; Radisic, M. Advanced Strategies for Modulation of the Material−Macrophage Interface. *Adv. Funct. Mater.* **2020**, *30* (44), 1909331.

(12) Stewart, C.; Akhavan, B.; Wise, S. G.; Bilek, M. M. M. A review of biomimetic surface functionalization for bone-integrating orthopedic implants: Mechanisms, current approaches, and future directions. *Prog. Mater. Sci.* **2019**, *106*, No. 100588.

(13) Tan, F.; Zhu, Y.; Ma, Z.; Al-Rubeai, M. Recent advances in the implant-based drug delivery in otorhinolaryngology. *Acta Biomater* **2020**, *108*, 46−55.

(14) Huo, K.; Xu, N.; Fu, J.; Chu, P. K. Bioactive inorganic-ion-doped titania nanotube coatings on bone implants with enhanced osteogenic activity and antibacterial properties. In *Nanobiomaterials in Clinical Dentistry*; Subramani, K.; Ahmed, W., Eds.; Elsevier: 2019; pp 401−427.

(15) Pakshir, P.; Younesi, F.; Wootton, K. A.; Battiston, K.; Whitton, G.; Ilagan, B.; Louka, D.; Statham, M.; Mackey, G.; Daley, A.; Parrag, I.; Naimark, W.; Hinz, B. Controlled release of low-molecular weight, polymer-free corticosteroid coatings suppresses fibrotic encapsulation of implanted medical devices. *Biomaterials* **2022**, *286*, No. 121586.

(16) Battiston, K.; Parrag, I.; Statham, M.; Louka, D.; Fischer, H.; Mackey, G.; Daley, A.; Gu, F.; Baldwin, E.; Yang, B.; Muirhead, B.; Hicks, E. A.; Sheardown, H.; Kalachev, L.; Crean, C.; Edelman, J.; Santerre, J. P.; Naimark, W. Polymer-free corticosteroid dimer implants for controlled and sustained drug delivery. *Nat. Commun.* **2021**, *12* (1), 2875.

(17) Farah, S.; Doloff, J. C.; Muller, P.; Sadraei, A.; Han, H. J.; Olafson, K.; Vyas, K.; Tam, H. H.; Hollister-Lock, J.; Kowalski, P. S.; Griffin, M.; Meng, A.; McAvoy, M.; Graham, A. C.; McGarrigle, J.; Oberholzer, J.; Weir, G. C.; Greiner, D. L.; Langer, R.; Anderson, D. G. Long-term implant fibrosis prevention in rodents and non-human primates using crystallized drug formulations. *Nat. Mater.* **2019**, *18* (8), 892−904.

(18) Battiston, K.; Parrag, I.; Statham, M.; Louka, D.; Fischer, H.; Mackey, G.; Daley, A.; Gu, F.; Baldwin, E.; Yang, B. Q.; Muirhead, B.; Hicks, E. A.; Sheardown, H.; Kalachev, L.; Crean, C.; Edelman, J.; Santerre, J. P.; Naimark, W. Polymer-free corticosteroid dimer

implants for controlled and sustained drug delivery. *Nat. Commun.* **2021**, *12* (1), 2875.
(19) Abaricia, J. O.; Farzad, N.; Heath, T. J.; Simmons, J.; Morandini, L.; Olivares-Navarrete, R. Control of innate immune response by biomaterial surface topography, energy, and stiffness. *Acta Biomater* **2021**, *133*, 58−73.
(20) Kang, H.; Jung, H. J.; Kim, S. K.; Wong, D. S. H.; Lin, S.; Li, G.; Dravid, V. P.; Bian, L. Magnetic Manipulation of Reversible Nanocaging Controls In Vivo Adhesion and Polarization of Macrophages. *ACS Nano* **2018**, *12* (6), 5978−5994.
(21) Hao, M.; Wang, W.; Kumar, A.; Kamaruddin, W. H. A.; Saidin, S.; Malek, N. A. N. N.; Claverie, J.; Liu, H. Magnetic hydroxyapatite nanobelt-stem cell hybrid spheroids for remotely patterning bone tissues. *BMEMat* **2023**, No. e12059.
(22) Lv, L.; Xie, Y.; Li, K.; Hu, T.; Lu, X.; Cao, Y.; Zheng, X. Unveiling the Mechanism of Surface Hydrophilicity-Modulated Macrophage Polarization. *Adv. Healthcare Mater.* **2018**, *7* (19), 1800675.
(23) Mordechay, L.; Le Saux, G.; Edri, A.; Hadad, U.; Porgador, A.; Schvartzman, M. Mechanical Regulation of the Cytotoxic Activity of Natural Killer Cells. *ACS Biomater Sci. Eng.* **2021**, *7* (1), 122−132.
(24) Du, H.; Bartleson, J. M.; Butenko, S.; Alonso, V.; Liu, W. F.; Winer, D. A.; Butte, M. J. Tuning immunity through tissue mechanotransduction. *Nature Reviews Immunology* **2023**, *23* (3), 174−188.
(25) Meli, V. S.; Atcha, H.; Veerasubramanian, P. K.; Nagalla, R. R.; Luu, T. U.; Chen, E. Y.; Guerrero-Juarez, C. F.; Yamaga, K.; Pandori, W.; Hsieh, J. Y.; Downing, T. L.; Fruman, D. A.; Lodoen, M. B.; Plikus, M. V.; Wang, W.; Liu, W. F. YAP-mediated mechanotransduction tunes the macrophage inflammatory response. *Sci. Adv.* **2020**, *6* (49), No. eabb8471.
(26) Chen, S.; Yang, J.; Wei, Y.; Wei, X. Epigenetic regulation of macrophages: from homeostasis maintenance to host defense. *Cell Mol. Immunol* **2020**, *17* (1), 36−49.
(27) Ivashkiv, L. B. Epigenetic regulation of macrophage polarization and function. *Trends Immunol* **2013**, *34* (5), 216−23.
(28) Jain, N.; Vogel, V. Spatial confinement downsizes the inflammatory response of macrophages. *Nat. Mater.* **2018**, *17* (12), 1134.
(29) Huse, M. Mechanical forces in the immune system. *Nature Reviews Immunology* **2017**, *17* (11), 679−690.
(30) Krzyszczyk, P.; Schloss, R.; Palmer, A.; Berthiaume, F. The Role of Macrophages in Acute and Chronic Wound Healing and Interventions to Promote Pro-wound Healing Phenotypes. *Front. Physiol.* **2018**, *9*, 419.
(31) Chen, S.; Saeed, A. F.; Liu, Q.; Jiang, Q.; Xu, H.; Xiao, G. G.; Rao, L.; Duo, Y. Macrophages in immunoregulation and therapeutics. *Signal Transduction Targeted Ther.* **2023**, *8* (1), 207.
(32) Mosser, D. M.; Edwards, J. P. Exploring the full spectrum of macrophage activation. *Nat. Rev. Immunol* **2008**, *8* (12), 958−69.
(33) Brown, B. N.; Londono, R.; Tottey, S.; Zhang, L.; Kukla, K. A.; Wolf, M. T.; Daly, K. A.; Reing, J. E.; Badylak, S. F. Macrophage phenotype as a predictor of constructive remodeling following the implantation of biologically derived surgical mesh materials. *Acta biomaterialia* **2012**, *8* (3), 978−987.
(34) Kzhyshkowska, J.; Gudima, A.; Riabov, V.; Dollinger, C.; Lavalle, P.; Vrana, N. E. Macrophage responses to implants: prospects for personalized medicine. *J. Leukoc Biol.* **2015**, *98* (6), 953−62.
(35) Wang, Y.; Shi, R.; Zhai, R.; Yang, S.; Peng, T.; Zheng, F.; Shen, Y.; Li, M.; Li, L. Matrix stiffness regulates macrophage polarization in atherosclerosis. *Pharmacol. Res.* **2022**, *179*, No. 106236.
(36) Sridharan, R.; Cavanagh, B.; Cameron, A. R.; Kelly, D. J.; O'Brien, F. J. Material stiffness influences the polarization state, function and migration mode of macrophages. *Acta Biomater* **2019**, *89*, 47−59.
(37) Wong, S. W.; Lenzini, S.; Cooper, M. H.; Mooney, D. J.; Shin, J. W. Soft extracellular matrix enhances inflammatory activation of mesenchymal stromal cells to induce monocyte production and trafficking. *Sci. Adv.* **2020**, *6* (15), No. eaaw0158.
(38) Fu, Y.; Jing, Z.; Chen, T.; Xu, X.; Wang, X.; Ren, M.; Wu, Y.; Wu, T.; Li, Y.; Zhang, H.; Ji, P.; Yang, S. Nanotube patterning reduces macrophage inflammatory response via nuclear mechanotransduction. *J. Nanobiotechnol.* **2023**, *21* (1), 229.
(39) Christo, S. N.; Bachhuka, A.; Diener, K. R.; Mierczynska, A.; Hayball, J. D.; Vasilev, K. The Role of Surface Nanotopography and Chemistry on Primary Neutrophil and Macrophage Cellular Responses. *Adv. Healthc Mater.* **2016**, *5* (8), 956−65.
(40) Unadkat, H. V.; Hulsman, M.; Cornelissen, K.; Papenburg, B. J.; Truckenmuller, R. K.; Carpenter, A. E.; Wessling, M.; Post, G. F.; Uetz, M.; Reinders, M. J.; Stamatialis, D.; van Blitterswijk, C. A.; de Boer, J. An algorithm-based topographical biomaterials library to instruct cell fate. *Proc. Natl. Acad. Sci. U. S. A.* **2011**, *108* (40), 16565−70.
(41) Ermis, M.; Antmen, E.; Hasirci, V. Micro and Nanofabrication methods to control cell-substrate interactions and cell behavior: A review from the tissue engineering perspective. *Bioact Mater.* **2018**, *3* (3), 355−369.
(42) Hulsman, M.; Hulshof, F.; Unadkat, H.; Papenburg, B. J.; Stamatialis, D. F.; Truckenmuller, R.; van Blitterswijk, C.; de Boer, J.; Reinders, M. J. Analysis of high-throughput screening reveals the effect of surface topographies on cellular morphology. *Acta Biomater* **2015**, *15*, 29−38.
(43) Zhu, Y.; Liang, H.; Liu, X.; Wu, J.; Yang, C.; Wong, T. M.; Kwan, K. Y. H.; Cheung, K. M. C.; Wu, S.; Yeung, K. W. K. Regulation of macrophage polarization through surface topography design to facilitate implant-to-bone osteointegration. *Sci. Adv.* **2021**, *7* (14), No. eabf6654.
(44) Park, R.; Kang, M. S.; Heo, G.; Shin, Y. C.; Han, D. W.; Hong, S. W. Regulated Behavior in Living Cells with Highly Aligned Configurations on Nanowrinkled Graphene Oxide Substrates: Deep Learning Based on Interplay of Cellular Contact Guidance. *ACS Nano* **2024**, *18* (2), 1325−1344.
(45) Mouw, J. K.; Ou, G.; Weaver, V. M. Extracellular matrix assembly: a multiscale deconstruction. *Nat. Rev. Mol. Cell Biol.* **2014**, *15* (12), 771−85.
(46) Humphrey, J. D.; Dufresne, E. R.; Schwartz, M. A. Mechanotransduction and extracellular matrix homeostasis. *Nat. Rev. Mol. Cell Biol.* **2014**, *15* (12), 802−12.
(47) Yang, L.; Conley, B. M.; Rathnam, C.; Cho, H. Y.; Pongkulapa, T.; Conklin, B.; Lee, K. B. Predictive Biophysical Cue Mapping for Direct Cell Reprogramming Using Combinatorial Nanoarrays. *ACS Nano* **2022**, *16* (4), 5577−5586.
(48) Yang, L.; Conley, B. M.; Yoon, J.; Rathnam, C.; Pongkulapa, T.; Conklin, B.; Hou, Y.; Lee, K. B. High-Content Screening and Analysis of Stem Cell-Derived Neural Interfaces Using a Combinatorial Nanotechnology and Machine Learning Approach. *Research* **2022**, *2022*, 9784273.
(49) Liu, R.; Cao, L.; Liu, D.; Wang, L.; Saeed, S.; Wang, Z. Laser Interference Lithography-A Method for the Fabrication of Controlled Periodic Structures. *Nanomaterials (Basel)* **2023**, *13* (12), 1818.
(50) Xie, Q.; Hong, M. H.; Tan, H. L.; Chen, G. X.; Shi, L. P.; Chong, T. C. Fabrication of nanostructures with laser interference lithography. *J. Alloys Compd.* **2008**, *449* (1−2), 261−264.
(51) Aufa, A. N.; Hassan, M. Z.; Ismail, Z. Recent advances in Ti-6Al-4V additively manufactured by selective laser melting for biomedical implants: Prospect development. *J. Alloys Compd.* **2022**, *896*, No. 163072.
(52) Zhao, J.; Chen, Z.; Liu, S.; Li, P.; Yu, S.; Ling, D.; Li, F. Nano-bio interactions between 2D nanomaterials and mononuclear phagocyte system cells. *BMEMat* **2024**, No. e12066.
(53) Su, D.; Jiao, Z.; Li, S.; Yue, L.; Li, C.; Deng, M.; Hu, L.; Dai, L.; Gao, B.; Wang, J.; Zhang, H.; Xiao, H.; Chen, F.; Yang, H.; Zhou, D. Spatiotemporal single-cell transcriptomic profiling reveals inflammatory cell states in a mouse model of diffuse alveolar damage. *Exploration* **2023**, *3* (3), 20220171.
(54) Xu, S.; Liu, Y.; Lee, H.; Li, W. Neural interfaces: Bridging the brain to the world beyond healthcare. *Exploration* **2024**, 20230146.

https://doi.org/10.1021/acsnano.4c04406
ACS Nano 2024, 18, 25465−25477

(55) Lee, M.; Du, H.; Winer, D. A.; Clemente-Casares, X.; Tsai, S. Mechanosensing in macrophages and dendritic cells in steady-state and disease. *Front. Cell Dev. Biol.* **2022**, *10*, 1044729.
(56) Meli, V. S.; Veerasubramanian, P. K.; Downing, T. L.; Wang, W.; Liu, W. F. Mechanosensation to inflammation: Roles for YAP/TAZ. in innate immune cells. *Sci. Signaling* **2023**, *16* (783), No. eadc9656.
(57) Wan, S.; Fu, X.; Ji, Y.; Li, M.; Shi, X.; Wang, Y. FAK- and YAP/TAZ dependent mechanotransduction pathways are required for enhanced immunomodulatory properties of adipose-derived mesenchymal stem cells induced by aligned fibrous scaffolds. *Biomaterials* **2018**, *171*, 107−117.
(58) Jain, N.; Vogel, V. Spatial confinement downsizes the inflammatory response of macrophages. *Nat. Mater.* **2018**, *17* (12), 1134−1144.
(59) Kuznetsova, T.; Prange, K. H. M.; Glass, C. K.; de Winther, M. P. J. Transcriptional and epigenetic regulation of macrophages in atherosclerosis. *Nature Reviews Cardiology* **2020**, *17* (4), 216−228.
(60) Benayoun, B. A.; Pollina, E. A.; Ucar, D.; Mahmoudi, S.; Karra, K.; Wong, E. D.; Devarajan, K.; Daugherty, A. C.; Kundaje, A. B.; Mancini, E.; Hitz, B. C.; Gupta, R.; Rando, T. A.; Baker, J. C.; Snyder, M. P.; Cherry, J. M.; Brunet, A. H3K4me3 breadth is linked to cell identity and transcriptional consistency. *Cell* **2014**, *158* (3), 673−88.

https://doi.org/10.1021/acsnano.4c04406
ACS Nano 2024, 18, 25465−25477